# Efficient kinetic particle simulations of space charge limited emission in magnetically insulated transmission lines using reduced physics models

E. G. Evstatiev* and M. H. Hess

*Sandia National Laboratories, Albuquerque, New Mexico 87185, USA*

(Received 3 May 2023; accepted 22 August 2023; published 8 September 2023)

We explore the use of reduced physics models for efficient kinetic particle simulations of space charge limited (SCL) emission in inner magnetically insulated transmission lines (inner MITLs), with application to Sandia National Laboratories' *Z* machine. We propose a drift kinetic (guiding center) model of electron motion in place of a fully kinetic model and electrostatic-magnetostatic fields in place of electromagnetic fields. The validity of these approximations is suggested by the operational parameters of the *Z* machine, namely, current pulse lengths of order 100 ns compared with Larmor periods typically smaller than $10^{-11}$ s, typical Larmor radii of a few (tens) of microns (magnetic fields of tens to hundreds of Tesla) compared with MITL dimensions of a few centimeters, and transient time of light waves along the inner MITL of order a fraction of a nanosecond. Guiding center orbits eliminate the fast electron gyromotion, which enables the use of tens to hundreds of times larger time steps in the numerical particle advance. Electrostatic-magnetostatic fields eliminate the Courant-Friedrichs-Lewy (CFL) numerical stability limit on the time step and allow the use of higher grid resolutions or, alternatively, larger time steps in the fields advance. Overall, potential computational cost savings of tens to hundreds of times exists. The applicability of the reduced physics models is examined on two problems. First, in the simulation of space charge limited emission of electrons from the cathode surface due to high electric fields in a radial inner MITL geometry with a short load. In particular, it is shown that a drift kinetic-based particle-in-cell (PIC) model with electrostatic-magnetostatic fields is able to accurately reproduce well-known physics of electron vortex formation, spatially and temporally. Second, deeper understanding is gained of the mechanism behind vortex formation in this MITL geometry by considering an exemplar problem of an electron block of charge. This simpler setup reveals that the main mechanism of vortex formation can be attributed to pure drift motion of the electrons, that is, the (fully kinetic) gyromotion of the electrons is inessential to the process. This exemplar problem also suggests a correlation of the spatial dimensions of vortices to the thickness of the electron layer, as observed in SCL simulations. It also confirms that the electromagnetic nature of the fields does not play an essential role. Finally, an improved hybrid fully kinetic and drift kinetic model for electron motion is proposed, as means of capturing finite Larmor radius (FLR) effects; the particular FLR physics that is missed by the drift kinetic model is the particle-wall interaction. By initializing SCL emitted electrons as fully kinetic and later transitioning them to drift kinetic, according to simple criteria, the accuracy of SCL simulations can be improved, while preserving the potential for computational efficiency.

DOI: 10.1103/PhysRevAccelBeams.26.090403

## I. INTRODUCTION

Sandia National Laboratories' *Z* machine [1,2], the world's most powerful accelerator, provides a platform for studying a wide variety of high energy density physics problems. An electromagnetic pulse is generated and transported via magnetically insulated transmission lines (MITLs) from a radius of 15m to a load of radius a few millimeters. When transporting a large amount of electromagnetic power, the last 5–10 cm, the so-called inner MITL, are subjected to extreme conditions that lead to the generation of low density plasmas and associated current losses [3–5]. Losses of 10% are routinely observed while 20% or more are possible.

To control and minimize these losses, numerical simulations are used in the design of MITLs. It has been established that physical processes under the extreme conditions in the inner MITL (high current densities, fields, and temperatures) are most accurately described by kinetic (nonthermal) models. Such kinetic simulations are presently done at Sandia via the particle-in-cell (PIC) method

*egevsta@sandia.gov

and are highly demanding of computational resources, requiring tens to hundreds of thousands of CPU hours, for example. The reasons for the high computational cost can be attributed to two main factors: (i) the fully kinetic (FK) model used in these codes, which necessitates resolving the small temporal and spatial scales of the helical motion of electrons in the high magnetic fields in the inner MITL (e.g., ~400 Tesla or more); and (ii) the electromagnetic (EM) nature of these codes, which imposes another limitation on the simulation time step via the Courant-Friedrichs-Lewy (CFL) condition. Therefore, a more computationally efficient alternative is desired.

This paper explores two reduced physics models designed to provide a more efficient kinetic alternative to the presently used PIC models. First, the drift-kinetic (DK) guiding center particle motion, which averages away the small temporal and spatial scales of the helical motion, could allow a DK-based PIC code to take tens or hundreds of times larger time steps. And second, the infinite speed of light limit, by using electrostatic and magnetostatic (ES-MS) fields,[1] which removes the CFL limiting condition on the time step. The main question this paper is concerned with is this: Can these reduced physics models represent sufficiently accurately the kinetic physics of space charge limited emission in the $Z$ inner MITL? Thus, a secondary purpose of this paper is to provide general insight into the dynamics of time dependent magnetic insulation. The vast body of previous research has focused on stationary, time independent magnetic insulation or offers limited results on time dependent flows [7–13]. We show that time dependence induces qualitative changes to the dynamics of the space charge limited (SCL) emission layer and that vortices play an essential role.

Recent work [6] has studied the motion of single electron particles in vacuum external fields and has found the two reduced models described above to be an excellent approximation. Based on these encouraging results, this paper continues to develop this idea and fills in the next missing piece in justifying the approach, i.e., includes self-consistent space charge effects. We use a test PIC code based on DK particle motion and ES-MS fields in two spatial dimensions (2D) in cylindrical coordinates with azimuthal symmetry to replicate well-known physics in the inner MITL, namely, the formation and evolution of self-organized vortical structures due to SCL field emission of electrons from the cathode. In Fig. 1, we show a comparison of simulations of SCL emission in the inner MITL with full kinetic and drift kinetic models, both with ES-MS fields, for a typical for the $Z$ machine 20 MA, 120 ns current pulse. For now, we only point out that both models show excellent agreement in the creation and properties of such vortices, as seen in the computational particle (henceforth, just particle) scatterplots and the number density plots.[2] Electrons in the particle scatterplots are colored according to their normalized to unity computational weights, information which could help identify regions of larger and smaller emission, as discussed later. We postpone detailed discussions of these results to the following sections.

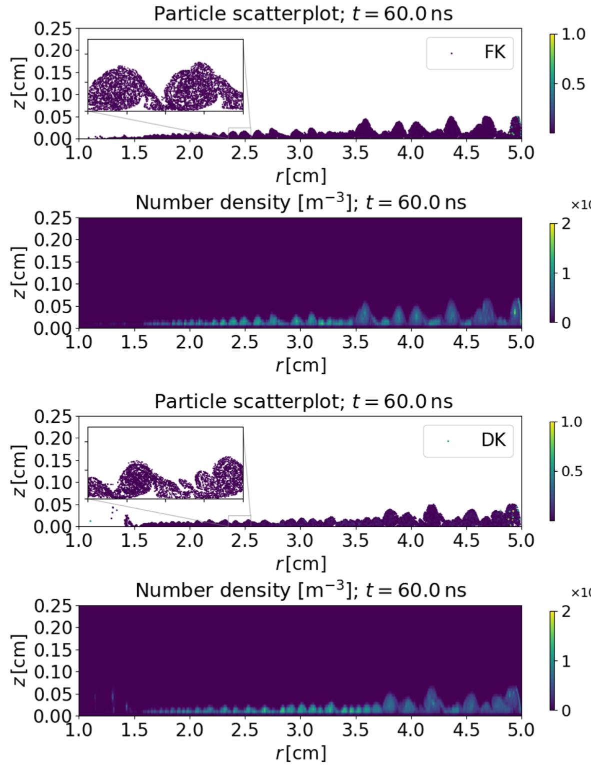


FIG. 1. Comparison of full kinetic (FK-PIC) and drift kinetic (DK-PIC) simulations with a sine squared current pulse [cf. Eq. (18)] of amplitude and length $I_{\mathrm{peak}} = 20$ MA and $\tau_{\mathrm{peak}} = 120$ ns, and ES-MS fields. The top panel shows full kinetic and the bottom panel drift kinetic PIC. Vortices of similar properties are clearly seen in both models. The color bar in the particle scatterplot indicates the normalized to unity computational particle weight.

To clarify the mechanism of vortex formation in the DK/ES-MS reduced models, an exemplar problem of an annular electron (non-neutral) block of charge [rectangular in 2D $(r, z)$ cylindrical coordinates] in an external magnetic field is studied in Sec. IV. It becomes clear that the main driving force in the vortex formation is due to the space charge (self-generated) electric fields. The latter, together with the external (vacuum) fields, produce the $\mathbf{E} \times \mathbf{B}$, as

[1]Strictly speaking, our use of the term electrostatic-magnetostatic only applies to the self-fields, while the external fields, which have $\nabla \times \mathbf{E} \neq 0$, could more accurately be characterized as "quasi-electrostatic-magnetostatic." For consistency with our previous publication, Ref. [6], we adhere to the electrostatic-magnetostatic terminology; see the next section for the precise model.

[2]Hereafter by density, we refer to number density, unless otherwise specified.

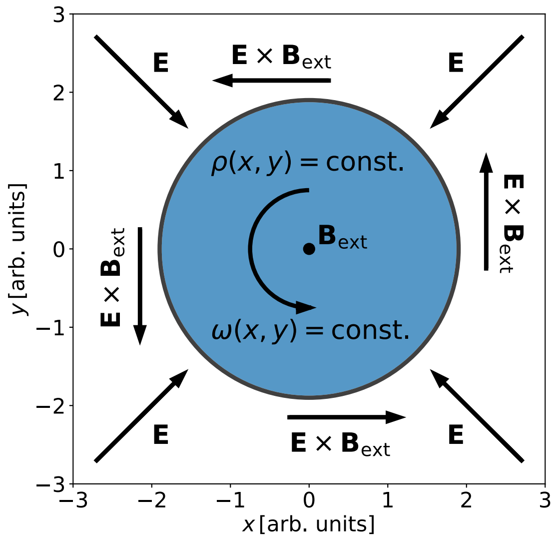


FIG. 2. A cartoon illustrating the existence of vortices in the drift kinetic model.

well as the less important $\nabla B$ and curvature drifts, which tend to wrap the initial rectangular configuration into vortical structures. The addition of time dependent external fields does not qualitatively alter this mechanism but, for example, the $\mathbf{E} \times \mathbf{B}$ drift becomes a driving factor of vortical motion. These conclusions are verified against a comparison with an identical initial configuration comprised of fully kinetic particles using both ES-MS and EM fields.

Space charge limited emission acts in a dynamically similar manner to the exemplar problem, undergoing the formation of multiple vortices within the SCL layer by a similar mechanism. Additionally, similar behavior to that in fluid vortex dynamics is observed in the form of vortex interactions (e.g., merging), vortex detachment from the cathode surface, etc. This type of dynamics is also verified by fully kinetic simulations with electromagnetic fields. Simulations in this work are performed with our DK and FK test PIC codes as well as with the PIC code CHICAGO [14–18].

We note that the existence of vortices within the drift kinetic model *per se* is not in question, as illustrated by the cartoon drawing in Fig. 2. The figure shows a simple setup with a constant negative charge density, $\rho(x, y) = \text{const.}$, within a circular region in Cartesian geometry. The space charge electric field is directed radially inward while the external magnetic field is constant and out of the page. The $\mathbf{E} \times \mathbf{B}$ drift causes all charges within the circle to move along circular trajectories and with the same angular velocity, $\omega(x, y) = \text{const.}$

The organization of this paper is as follows: Sec. II describes the theory of the drift kinetic model used in this work as well as details of its numerical implementation. Section III presents simulations of SCL emission and comparisons between fully kinetic and drift kinetic models. Section IV presents further tests and comparisons of the reduced and full physics models in a more controlled manner, using an exemplar problem of an electron block. Section V presents a hybrid full kinetic and drift kinetic model and discusses its advantages. Section VI concludes.

## II. THE DRIFT KINETIC MODEL

MITL geometries with azimuthal symmetry, or close to azimuthal symmetry, are commonly utilized in pulsed power experiments. In this section, we develop the self-consistent drift kinetic model for particles and fields in two spatial dimensions, in cylindrical coordinates $(r, \phi, z)$, with ignorable angular coordinate, $\phi$. This model is used in all drift kinetic simulations in the present work.

Azimuthal symmetry implies no dependence on the azimuthal angle $\phi$; for example, the electric scalar and magnetic vector potentials only depend on radial and axial coordinates, $\varphi(r, z)$ and $(A_r(r, z), A_\phi(r, z), A_z(r, z))$. The particular regime of interest in the present work is for a sufficiently strong magnetic field that ensures magnetic insulation of electrons. Accordingly, we make a few further simplifying assumptions: (i) that the azimuthal component of the vector potential identically vanishes, $A_\phi(r, z) \equiv 0$. Such assumption implies that the magnetic field, $\mathbf{B} = \nabla \times \mathbf{A}$ has only one nonzero component, $B_\phi(r, z) = \partial_z A_r - \partial_r A_z$, hence, a constant direction $\hat{\mathbf{b}} = \mathbf{B}/B = (0, 1, 0)$; (ii) that the non-neutral (electron) plasma currents are negligible in comparison with wall currents; and (iii) that MITL dimensions are small enough, e.g., a few centimeters, so that electromagnetic waves need not be considered. Although the last two assumptions are utilized in our numerical simulations, the equations below are derived in a slightly more general case, then specialized to assumptions (ii) and (iii). The most general case of azimuthal symmetry, which has nonzero $A_\phi(r, z)$ and includes the full plasma currents, will be the subject of future work.

The derivation follows Ref. [19], accounting for the above assumptions. The approach utilizes the phase space action principle, starting from a Lagrangian for drift kinetic particles and fields, in Coulomb gauge ($\nabla \cdot \mathbf{A} = 0$):

$$\begin{aligned}\mathcal{L}_{\mathrm{DK}} = &\sum_{\alpha=1}^{N_p} w_\alpha [q_s \mathbf{A} + m_s U_\alpha \hat{\mathbf{b}}] \cdot \dot{\mathbf{X}}_\alpha + \frac{m_s}{q_s} \sum_{\alpha=1}^{N_p} w_\alpha \mu_\alpha \dot{\Psi}_\alpha \\ &- \sum_{\alpha=1}^{N_p} w_\alpha \left[ q_s \varphi + \mu_\alpha B + \frac{m_\alpha U_\alpha^2}{2} \right] \\ &+ \int dx^3 \left\{ \frac{\epsilon_0}{2} \left[ -\varphi \nabla^2 \varphi + \left( \frac{\partial \mathbf{A}}{\partial t} \right)^2 \right] + \frac{1}{2\mu_0} \mathbf{A} \cdot \nabla^2 \mathbf{A} \right\},\end{aligned} \tag{1}$$

where the field terms have been integrated by parts. The remaining notation is as follows: $N_p$ is the total number of particles, $w_\alpha$ is the computational particle weight, $B = \sqrt{\mathbf{B}\cdot\mathbf{B}}$ is the magnitude of the magnetic field, $\mathbf{X}_\alpha$ is particle position, $U_\alpha$ is particle velocity in the direction of the magnetic field $\hat{\mathbf{b}}$, $\mu_\alpha = m_s v_{\alpha\perp}^2/2B$ is the magnetic moment of the drift kinetic particle, where $v_{\alpha\perp}$ is the particle's velocity perpendicular to the magnetic field, $\Psi_\alpha$ is the (fast) gyrophase of the particle, and $\epsilon_0$ and $\mu_0$ are the permittivity and permeability of vacuum. A dot denotes a time derivative. The subscript "s" denotes the species number; in our case, there is only electron species with charge $q_s = -e$ and mass $m_s = m_e$.

Note that in the phase space variational principle, a particle's velocity and the time derivative of its position are considered independent; that is, one performs independent variations with respect to both, $\mathbf{X}_\alpha$ and $U_\alpha$. The other independent variables that are varied to obtain the equations of motion are $\Psi_\alpha$, $\mu_\alpha$, and the fields $\varphi$ and $\mathbf{A}$.

A general remark about the model (1) is that it includes electromagnetic waves. Although in the present work, we argue that the electromagnetic nature of the fields is unimportant because of the small dimensions of the considered inner MITLs, in certain situations, such as the long coaxial MITL geometry studied in Ref. [20], the transient time (the wave going back and forth along the length of the MITL) is not negligible compared to the current pulse length, and using the electromagnetic fields would be the appropriate model.

We now make a reduction to two spatial dimensions with azimuthal symmetry in cylindrical coordinates. The guiding center particle coordinates are denoted by $(R, \Phi, Z)$, then the particle position is given by $\mathbf{X} = R\hat{r} + Z\hat{z}$ and its velocity by $\dot{\mathbf{X}} = \dot{R}\,\hat{r} + R\dot{\Phi}\,\hat{\phi} + \dot{Z}\,\hat{z}$, where $(\hat{r}, \hat{\phi}, \hat{z})$ are the three units vectors along the corresponding directions. As usual, the electric field is given by $\mathbf{E}(r,z) = -\partial_t\mathbf{A} - \nabla\varphi$. Substitution in (1) leads to the reduced drift kinetic Lagrangian

$$\begin{aligned}\mathcal{L}_{\mathrm{DK}} = {} & \sum_{\alpha=1}^{N_p} w_\alpha[q_s A_r(R_\alpha, Z_\alpha)\dot{R}_\alpha + q_s A_z(R_\alpha, Z_\alpha)\dot{Z}_\alpha \\ & + m_s U_\alpha R_\alpha \dot{\Phi}_\alpha] + \left(\frac{m_s}{q_s}\right)\sum_{\alpha=1}^{N_p} w_\alpha \mu_\alpha \dot{\Psi}_\alpha \\ & - \sum_{\alpha=1}^{N_p} w_\alpha\left[q_s\varphi(R_\alpha, Z_\alpha) + \mu_\alpha B(R_\alpha, Z_\alpha) + \frac{m_s U_\alpha^2}{2}\right] \\ & + \int drdz 2\pi r\left\{\frac{\epsilon_0}{2}\left[-\varphi(r,z)\nabla^2\varphi(r,z) \right.\right. \\ & \left.\left. + \left(\frac{\partial\mathbf{A}(r,z)}{\partial t}\right)^2\right] + \frac{1}{2\mu_0}\mathbf{A}(r,z)\cdot\nabla^2\mathbf{A}(r,z)\right\}. \end{aligned} \quad (2)$$

To derive the equations of motion for the particles, we first vary with respect to $Z_\alpha$ and obtain the following equation for $R_\alpha$:

$$\dot{R}_\alpha = \frac{1}{B_\phi}\left(\frac{\partial A_z}{\partial t} + \frac{\partial\varphi}{\partial Z_\alpha}\right) + \frac{\mu_\alpha}{q_s}\frac{1}{B_\phi}\frac{\partial B_\phi}{\partial Z_\alpha}. \quad (3)$$

Variation with respect to $R_\alpha$ gives the equation for $Z_\alpha$

$$\begin{aligned}\dot{Z}_\alpha = {} & -\frac{1}{B_\phi}\left(\frac{\partial A_r}{\partial t} + \frac{\partial\varphi}{\partial R_\alpha}\right) - \frac{\mu_\alpha}{q_s}\frac{1}{B_\phi}\frac{\partial B_\phi}{\partial R_\alpha} \\ & + \frac{m_s}{q_s}\frac{1}{B_\phi}U_\alpha\dot{\Phi}_\alpha. \end{aligned} \quad (4)$$

Next, variation with respect to $\Phi_\alpha$ gives:

$$\frac{d}{dt}(w_\alpha m_s U_\alpha R_\alpha) = 0 \quad \text{or} \quad w_\alpha m_s U_\alpha R_\alpha = \text{const.} = 0. \quad (5)$$

The choice of zero for the constant in Eq. (5) is necessary to ensure that the azimuthal component of the vector potential vanishes, $A_\phi \equiv 0$. Since a particle's radial coordinate, $R_\alpha(t)$, is a nonvanishing function of time, we obtain that

$$U_\alpha(t) = 0, \quad (6)$$

which also implies the choice for the initial value $U_{0\alpha} = 0$. The last equation of motion for $\Phi_\alpha$ is given by a variation with respect to $U_\alpha$:

$$\dot{\Phi}_\alpha = \frac{U_\alpha}{R_\alpha} = 0 \quad \text{or} \quad \Phi_\alpha(t) = \Phi_{0\alpha} = 0, \quad (7)$$

where (6) was used, and the last assumption was made without loss of generality. Substitution of (7) in (4) gives the final form

$$\dot{Z}_\alpha = -\frac{1}{B_\phi}\left(\frac{\partial A_r}{\partial t} + \frac{\partial\varphi}{\partial R_\alpha}\right) - \frac{\mu_\alpha}{q_s}\frac{1}{B_\phi}\frac{\partial B_\phi}{\partial R_\alpha}. \quad (8)$$

The $\mathbf{E}\times\mathbf{B}$ drift can be identified as the terms in parentheses in Eqs. (3) and (8), the terms with $\mu_\alpha$ represent $\nabla B$ drift, while the curvature drift vanishes after all symmetries and assumptions are included. Variation with respect to the gyrophase gives the conservation of magnetic moment, $\dot{\mu}_\alpha = 0$, and variation with respect to the magnetic moment gives an equation for the fast gyrophase $\dot{\Phi}_\alpha = (q_s/m_s)B$, which decouples from the rest of the equations and is typically not solved.

Next, the field equations are derived. Variation (functional derivative) with respect to the electric potential gives Poisson's equation:

$$\nabla^2\varphi(r,z) = -\frac{1}{2\pi r}\frac{\rho(r,z)}{\epsilon_0}, \quad (9)$$

where the charge density $\rho(r,z)$ is estimated from the particles positions (see below).

The last equation in our model is for the magnetic vector potential and is obtained from a variation of (2) with respect to $\mathbf{A}$:

$$\nabla^2 \mathbf{A}(r,z) - \frac{1}{c^2}\frac{\partial^2 \mathbf{A}(r,z)}{\partial t^2} = -\frac{\mu_0}{2\pi r}\sum_{\alpha=1}^{N^p} w_\alpha q_s \dot{\mathbf{X}}_\alpha, \tag{10}$$

with $\dot{\mathbf{X}}_\alpha = (\dot{R}_\alpha, \dot{Z}_\alpha)$. Note that all contributions to the current due to magnetization terms, as derived in Ref. [19], are missing from Eq. (10) due to the extra simplifying assumptions made above; however, these contributions would not vanish in the most general azimuthally symmetric formulation.

As already mentioned, one additional simplifying assumption was made that the plasma currents are negligible and only electrostatic and magnetostatic fields are used. Accordingly, we set the plasma and displacement currents to zero in Eq. (10), which then becomes the Laplace's equation for the vector potential:

$$\nabla^2 \mathbf{A}(r,z) = 0. \tag{11}$$

An additional consequence of the extra simplifying assumptions is that because the force equation, i.e., the equation for $U_\alpha$, has been eliminated, certain plasma physics is missing from the model, most notably, plasma oscillations. The lack of plasma oscillations in the direction of the magnetic field is certainly something to keep in mind; at the same time, it can be advantageous in numerical computations since explicit time integrators do not have a restriction on the time step due to numerical instabilities arising from underresolving the plasma frequency.

To summarize, the self-consistent drift kinetic particles and fields model is given by Eqs. (3), (8), (9), and either (10) or (11).

The total energy of particles and fields is given by

$$\begin{aligned} W_{\mathrm{DK}} = &\sum_{\alpha=1}^{N_p} w_\alpha\left[\frac{m_s}{2}U_\alpha^2 + \mu_\alpha B\right] \\ &+ \int drdz 2\pi r\left\{\frac{\epsilon_0}{2}\left[-\varphi\nabla^2\varphi + \left(\frac{\partial \mathbf{A}}{\partial t}\right)^2\right]\right. \\ &\left. - \frac{1}{2\mu_0}\mathbf{A}\cdot\nabla^2\mathbf{A}\right\}, \end{aligned} \tag{12}$$

where again, the field term $(\partial_t \mathbf{A})^2$ is included for the sake of generality, although in our ES-MS fields model it vanishes.

When using finite size particles in Eq. (1), one introduces a computational particle shape, $S$ (also referred to as an interpolating function). For a spatial discretization on a uniform mesh, as is our case, $S$ may be chosen as one of the spline functions listed in Refs. [21,22]. Our particle shape of choice is the quadratic spline, which has a continuous first derivative. For specifics on using particle shapes in energy conserving methods based on variational principles, we refer the reader to Refs. [19,23]. A two dimensional $S$ is simply a Cartesian product of two one dimensional $S$ functions.

After discretizing the field quantities on a grid, the charge density is accumulated on the grid with the help of the particle shape and Poisson's equation can be written as

$$\nabla^2_{ij;kl}\varphi_{kl} = -\sum_{\alpha=1}^{N_p}\frac{w_\alpha q_s}{\epsilon_0}\frac{S(r_{ij}-R_\alpha, z_{ij}-Z_\alpha)}{2\pi r_{ij}}, \tag{13}$$

where $i$, $j$, $k$, $l$ are grid indexes. The particle shape function satisfies the partition of unity property $\sum_{ij} h_r h_z S(r_{ij} - R_\alpha, z_{ij} - Z_\alpha) = 1$ (inherited from the same property in one spatial dimension), where $h_r$ and $h_z$ are the grid spacings in the $r$ and $z$ direction, respectively.

As usual, fields are interpolated to the particle position with the shape function $S$ while in energy conserving methods [19,23] derivatives are interpolated with the derivative of the shape function, for example

$$\left.\frac{\partial\varphi}{\partial r}\right|_{(R_\alpha,Z_\alpha)} \equiv \frac{\partial\varphi}{\partial R_\alpha} = h_r h_z \sum_{ij}\frac{\partial S(r_{ij}-R_\alpha, z_{ij}-Z_\alpha)}{\partial R_\alpha}\varphi_{ij}. \tag{14}$$

Because for the vector potential we will only be using analytic expressions (see the following section), the evaluation of the external fields at the particle position is done analytically, i.e., the shape function is not used.

### Radial MITL geometry

For simplicity of the discussion in this work, we specialize our geometry to a purely radial feed. The geometry is constrained by a load at $r_l = 1$ cm and a wall at the wave injection side at $r = 5$ cm. The cathode surface is at $z = 0$, while the anode is at either $z = 0.5$ cm or at 1 cm. The boundary conditions for the electric potential are zero Dirichlet on all sides.

In the radial MITL geometry, the vector potential has only one nonzero component, which depends on the $r$-coordinate alone, $A_z(r)$. This implies that the second term (containing $\mu_\alpha$) in Eq. (3) vanishes. Further, Ref. [6] shows that Eq. (11) is satisfied by the following analytic expression for the vector potential,

$$A_z(t,r) = \frac{\mu_0 I(t)}{2\pi}\log\left(\frac{r}{r_l}\right), \tag{15}$$

which leads to the following external field expressions:

$$\mathbf{B}_{\mathrm{ext}}(r,t) = -\frac{\mu_0 I(t)}{2\pi r}\hat{\phi}, \tag{16}$$

$$\mathbf{E}_{\rm ext}(r,t) = -\frac{\mu_0 \dot{I}(t)}{2\pi}\ln\left(\frac{r}{r_l}\right)\hat{z}. \quad (17)$$

All simulations are performed with either constant current (zero external electric field) or a sine squared shape,

$$I(t) = I_{\rm peak}\sin^2\left(\frac{\pi t}{2\tau_{\rm peak}}\right). \quad (18)$$

We note that the external electric field (17), being derived from a vector potential, is not conservative. Thus, for example, the frequently used in the literature "voltage," $V = -\int E dl$, where $E$ includes both the external and space charge fields, does *not* have the conservative properties of an electric potential, such as $\varphi$.

Our simulations typically include a relativistic factor $\gamma = 1/\sqrt{1 - v^2/c^2}$ in the denominator of the second term in Eq. (8), i.e., $\mu_\alpha \to \gamma\mu_\alpha$; however, for the typical observed velocities $\sim 0.1c$, we have not seen any significant relativistic effects.

As a last remark in this section, we note that some of our assumptions can be more rigorously justified for equilibrium Brillouin flows in general cross-fields devices, including in our radial geometry [24]. (We also note Ref. [25], which discusses two-species Brillouin flows.) In particular, that reference shows that for the regime of operation assumed here, plasma (electron) currents can be neglected in comparison with wall currents as well as that electrons are typically non- or weakly relativistic.

## III. PARTICLE SIMULATIONS OF SCL EMISSION

Space charge limited emission of electrons from the cathode occurs when the electric field magnitude near the surface exceeds a certain threshold value, e.g., 24 MV/m [20]. There is an important difference between an electron initialized at that threshold value, corresponding to the vacuum electric field, and the value of the electric field near the cathode surface after an electron layer has formed, as in the case of space charge limited emission. Specifically, after an SCL layer has formed, the value at which an electron is emitted is much smaller, with numerically observed values of the order ~0.5–1 MV/m. This difference is important since it determines the initial energy and momentum of an emitted electron. For example, one expects a high energy population of electrons to be emitted before an electron layer builds up. This small population of high energy electrons is expected to be poorly approximated by the drift kinetic model due to having larger than average Larmor radii. In the subsequent time evolution, and for the vast majority of the current pulse, one expects electrons to be emitted with much lower energy and momentum. For smaller initial energy and momentum, the emitted electrons have much smaller Larmor radii and are thus expected to be much more accurately approximated by the drift kinetic model. (Of course, "large" and "small" Larmor radii are understood in relation to the other relevant length scales in the drift kinetic theory [26].)

The numerical algorithm of the SCL model implemented in our test codes (DK-PIC and FK-PIC with ES-MS fields) has been borrowed from Ref. [27] (see also [28]). Electrons in the full kinetic code are initialized with zero initial kinetic energy at the first cell above the cathode surface, and subsequently accelerate due to the local nonzero value of the electric field. The initialization of drift kinetic electrons needs special attention. The initial data needed to initialize the motion of a drift kinetic electron is given by the initial position and the magnetic moment (we remind the reader that the initial velocity along the magnetic field is zero). The initial position of an emitted electron is chosen at a random radial location within the emitting cell. The magnetic moment is constant in the drift kinetic model and needs only be calculated and assigned once. We utilize two methods of magnetic moment initialization. The first one is by numerical computation: two Larmor periods are followed in the "frozen" electric and magnetic fields, using a full kinetic particle push. The full kinetic data is then used to compute the magnetic moment as

$$\mathbf{v}_d = \langle \mathbf{v} \rangle, \quad (19)$$

$$\mathbf{v}_{\rm osc} = \mathbf{v} - \mathbf{v}_d, \quad (20)$$

$$\mu = \left\langle \frac{m\mathbf{v}_{\rm osc}^2}{2B} \right\rangle, \quad (21)$$

where $\langle\rangle$ denotes time averaging. In the second method, the magnetic moment is computed from the fields as $\mu = m_e E^2/2B^3$ [6], where the electric field includes both the external and space charge contributions. Numerically computed magnetic moments are used in all simulations except in Sec. IV, where the analytical expression was used.

In all SCL simulations, the cathode emitting surface is in the range $1 \le r \le 5$ cm. All SCL simulations were performed with a sine squared current pulse profile given by (18) and with the external fields (16), (17). Most simulations were performed with a peak current $I_{\rm peak} = 2$ MA and a pulse length $\tau_{\rm peak} = 30$ ns. Under such parameters, the electrons still magnetically insulate while simulation times are an order of magnitude shorter than the typical time for the $Z$ machine current pulse with $I_{\rm peak} = 20$ MA and $\tau_{\rm peak} = 120$ ns.

Trajectories in the FK-PIC code were integrated in time with a relativistic Boris method [29] while the DK-PIC equations were integrated with a velocity Verlet method [30]. The time step for the 2MA peak current pulse was $dt = 2.5 \times 10^{-14}$ s in the FK-PIC and $dt = 2.5 \times 10^{-13}$ s in DK-PIC, i.e., 10 times larger in the drift kinetic model. The time step used for the 20MA current pulse in Fig. 1 was

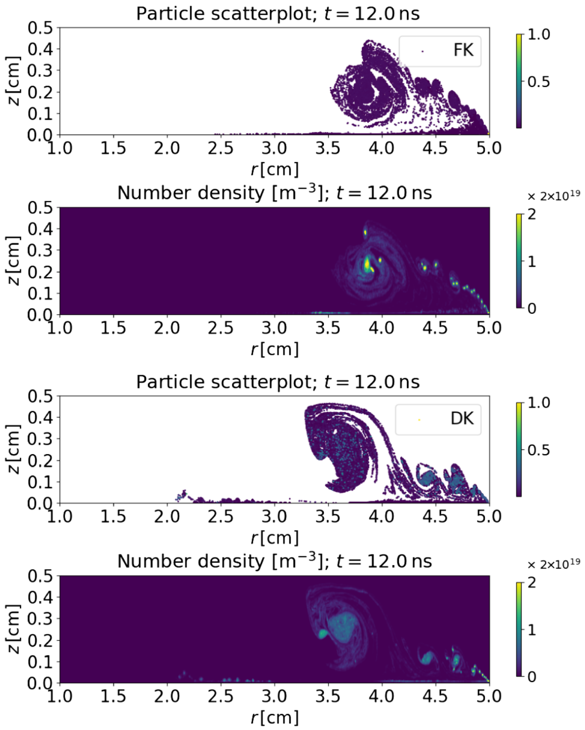


FIG. 3. An illustration of the formation of free floating vortices in both FK-PIC and DK-PIC due to the sharp boundary of the emission surface at 5 cm; parameters for this simulation are $I_{\mathrm{peak}} = 2$ MA and $\tau_{\mathrm{peak}} = 30$ ns.

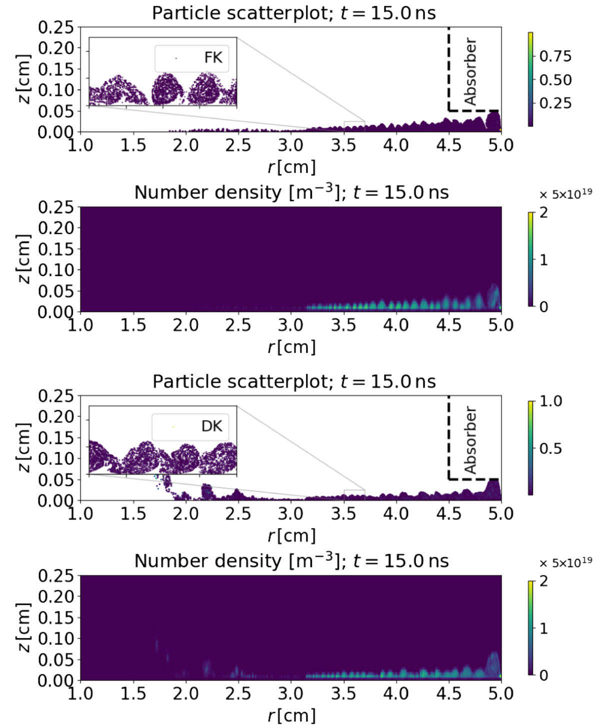


FIG. 4. Comparison of a full kinetic and drift kinetic simulations at 15 ns with $I_{\mathrm{peak}} = 2$ MA and $\tau_{\mathrm{peak}} = 30$ ns. After magnetic insulation sets in, the vortical structures are similar to those in Fig 1, where a higher peak current and longer pulse were used.

$dt = 5 \times 10^{-15}$ s for FK-PIC and again $dt = 2.5 \times 10^{-13}$ s for DK-PIC, i.e., 50 times larger in the drift kinetic model.

We now comment on an artifact in the numerical setup of SCL emission. The abrupt boundary of the emission surface at $r = 5$ cm is clearly not physical since the inner MITL extends past that radial distance and connects to the convolute. Therefore in reality, the threshold for SCL emission is first exceeded somewhere outside of our simulation domain. A property of SCL emission from a finite region is that it has a sharp peak at the ends of the emitting region, as shown in Refs. [27,28]. Numerically, this manifests in disproportionately large emission in the first few cells of large amounts of charge via electrons with high energies. Such large emission typically leads to the accumulation of a large amount of charge in the form of large "free floating" vortices, an example of which is shown in Fig. 3. The large amount of charge in these vortices generates large electric fields and disrupts the course of the SCL emission from the rest of the emitting cathodes surface. Such charge evolution clearly does not represent the more physically realistic simulation, which should include both the inner MITL and the convolute.

To mitigate this artifact, we place an (artificial) absorbing block (see Fig. 4), which absorbs all electrons with coordinates $r \geq 4.5$ cm and $z \geq 0.5$ mm. This simple setup prevents large, free floating vortices from forming in all presented simulations. More sophisticated algorithms have been devised in other codes, using temporal and spatial ramps and fractional charge injection [5,31]; nevertheless, our simple solution suffices for the purposes of the present work.

Figure 4 shows a full kinetic (top panel) and a drift kinetic (bottom panel) simulation comparison of SCL cathode emission, for a current pulse with $I_{\mathrm{peak}} = 2$ MA and $\tau_{\mathrm{peak}} = 30$ ns. The most important feature of this comparison is that the vortical structures observed in both simulations are similar to those in Fig. 1. Details of the vortical structures are reproduced with excellent agreement by the drift kinetic simulation, including the sizes (e.g., larger vortices at larger radii and smaller vortices at smaller radii) and timing of vortex formation (more detailed analysis follows). The formation of these vortices cannot be due to full kinetic particle gyromotion since the DK model lacks such completely. In fact, the Larmor radii of the fully kinetic electrons are of the order 5–50 μm or less, while the vortex dimensions are of the order ~100–300 μm. Therefore, we conclude that the primary mechanism of vortex formation must be due to the *drift motion* of particles.

Another noteworthy feature of Fig. 4 is that particles exist in the radial range $r \leq 3.14$ cm (these particles also are seen to form vortices). The reason to note this is that the electric field on the cathode surface below $r \simeq 3.14$ cm never exceeds the threshold value of 24 MV/m and, therefore, these particles must have been "born" upstream. The most likely location of their origin is the first few cells, close to $r = 5$ cm, since particles emitted there have typically higher energy, allowing their fast propagation radially downstream by the $\mathbf{E} \times \mathbf{B}$ drift. We will return to the discussion of this particle population.

Although the similarities between FK-PIC and DK-PIC in Fig. 4 are clear, the two simulations are not identical. The vortical structures are a sign of a highly nonlinear system with a high degree of sensitivity to the initial conditions (chaos). Therefore, statistical analysis is necessary to systematically study similarities and differences. To such effect, an ensemble of ten simulations were performed with each model. The individual samples within each group differ by the random initial particle placement within an emitting cell; such source of randomness is sufficient to drive the temporal evolution of each sample in a uniquely different way. The spatial structure is examined in the restricted range $3.1 \le r \le 4.5$ cm due to the above described emission artifact and the related absorber "fix." In Fig. 5, we show a Fourier analysis of the first 6 modes $k = \pm 2\pi n/\Delta L$ with an integer $n = 0, 1, \ldots, 5$ and $\Delta L = 4.5 - 3.1 = 1.4$ cm, for 3 times, 10, 15, and 20 ns. The averages of all simulations are shown by the thick blue and green curves. The individual sample runs are shown in dashed lines and give an idea of the data spread. We observe that the $n = 0$ mode, representing the total charge withing the range, has somewhat good agreement at 10 ns and very good agreement at 15 ns and 20 ns. Modes $n =$ 1–5 show very good agreement and confirm that spatially (and temporally, at the three times) the vortical structures formed in full kinetic and drift kinetic simulations are in excellent agreement.

The next Fig. 6 shows the total charge and total kinetic energy of particles in the same $r$-range, as a function of time; Fig. 7 shows the same quantities in the system i.e., includes the full $r$-range. We see that the stochastic behavior of the vortices begins to manifest past ~10 ns (also true outside of the considered $r$-range). We confirm that at 10 ns the DK model overestimates the total charge (mode $n = 0$ in Fig. 5) and that there is closer agreement at $t = 15$ and 20 ns. Lastly, we see that past about 25 ns the DK model retains slightly more charge than the FK model.

As a general remark, we point out that the directional motion of vortices is predominantly in the negative $r$-direction (inward, toward the load) for the first ~15 ns, or about half of the pulse peak, after which the general direction reverses and vortices start moving in the positive $r$ direction (outward). Once the outward motion commences, electrons are lost to the boundary of the domain at $r = 5$ cm, leading to subsequent decrease in the total charge and kinetic energy in the simulation. The reversal of the directional motion of vortices can be understood in the following way. For our sine squared pulse, the maximum of the external electric field is at quarter length of the pulse, i.e., $\tau_{\mathrm{peak}}/2$. After this time, the external electric field starts decreasing while the electric field of the SCL electron layer (space charge) near the cathode remains

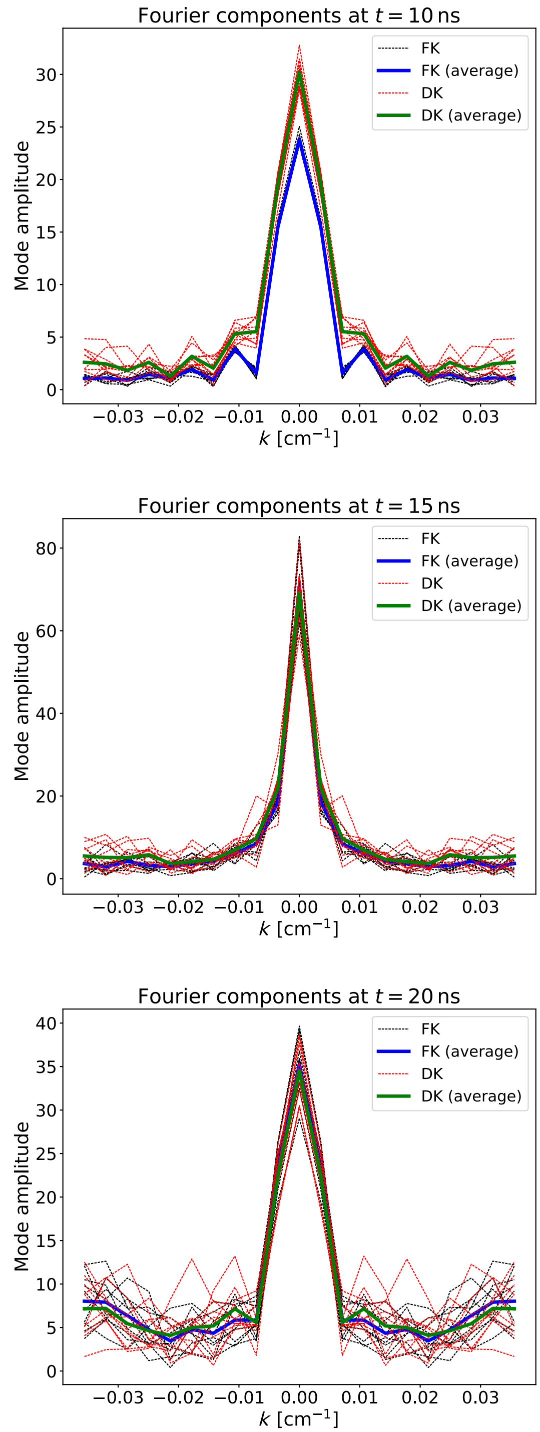


FIG. 5. Comparison of Fourier components of the density lineout $z = 100$ μm, $3.1 \le r \le 4.5$ cm, in full kinetic and drift kinetic simulations with $I_{\mathrm{peak}} = 2$ MA and $\tau_{\mathrm{peak}} = 30$ ns. The thick lines are the averages of ten simulations with random emission positions.

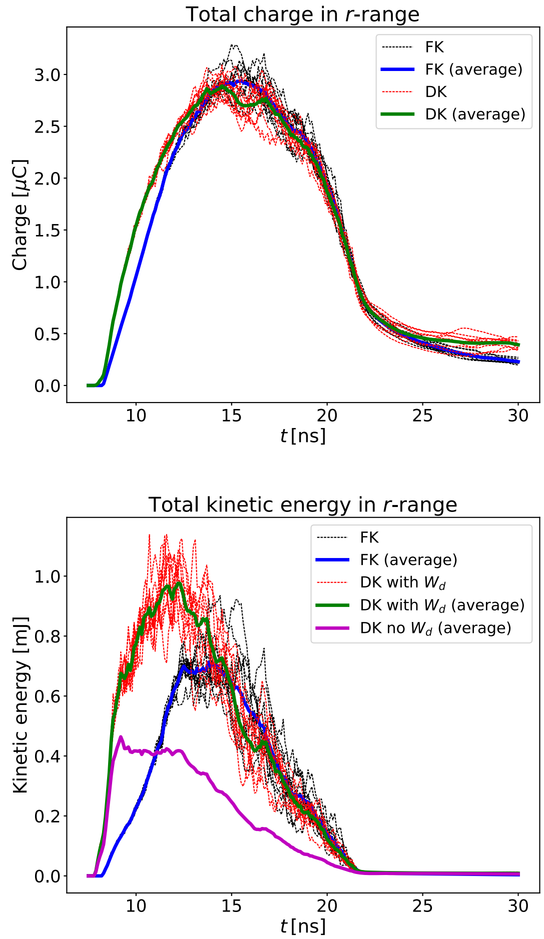


FIG. 6. Comparison of total charge and total particle kinetic energy in full kinetic and drift kinetic simulations in the radial range $3.1 \le r \le 4.5$ cm with $I_{\mathrm{peak}} = 2$ MA and $\tau_{\mathrm{peak}} = 30$ ns. The thick lines are the averages of ten simulations with random emission positions.

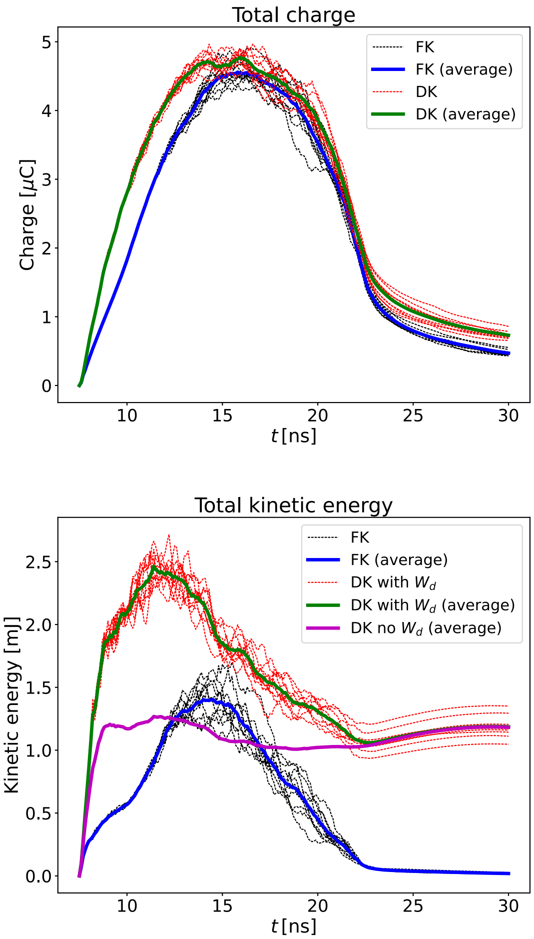


FIG. 7. Comparison of total charge and total particle kinetic energy in full kinetic and drift kinetic simulations with $I_{\mathrm{peak}} = 2$ MA and $\tau_{\mathrm{peak}} = 30$ ns. The thick lines are the averages of ten simulations with random emission positions.

unchanged (the SCL layer does not immediately lose charge). In this manner, the space charge field begins to dominate the external electric field. But the space charge electric field has opposite direction to that of the external field, i.e., the total electric field near the cathode reverses direction. The reversed electric field near the cathode reverses the direction of the $\mathbf{E} \times \mathbf{B}$ drift and causes vortices to start moving out of the system, in the positive $r$ direction.

The total kinetic energy in Figs. 6 and 7 deserves a further discussion due to the apparent disagreement in its temporal dependence between the two models. The averaged curve of the FK-PIC is the thick blue line, as before, and the averaged DK-PIC curves are now two, a thick green line labeled as "DK with $W_d$ (average)" and a thick magenta line labeled "DK no $W_d$ (average)." $W_d$ refers to the kinetic energy due to the guiding center motion, as opposed to the kinetic energy contained in the perpendicular Larmor oscillation. We now discuss the contribution of $W_d$.

A first observation is that the curves including $W_d$ have better agreement than the curves without $W_d$. There is a subtlety in this comparison. The first question that comes to mind is why include the guiding center drift energy since this energy is not present in the drift kinetic model—see the first term in the square brackets in Eq. (12). Indeed, the drift kinetic model derived in Refs. [19,26] assumes a specific ordering in defining the small parameter of the theory, in which the electric field is small compared to the magnetic field. As a consequence, the drift motion is assumed to be much slower than the circular motion, rendering the drift velocity (and the associated drift motion kinetic energy) of higher order in the small parameter. Hence, the kinetic energy due to the drift motion of particles is not included in the energy balance in the DK model. However, when applying the drift kinetic model to our problem of electrons emitted at a *finite* $E_{\mathrm{th}}$, it turns out that this drift motion is not negligible for the first few nanoseconds. At the heart of this apparent discrepancy lies the fact that $E_{\mathrm{th}}$ for SCL emission is quite large, and together with the magnetic field $B$ at the moment of emission, makes the $\mathbf{E} \times \mathbf{B}$ drift dominant among the three drifts at the initial time. (We remind the reader that the curvature drift is identically zero in our model.) Considering the $\mathbf{E} \times \mathbf{B}$ drift outside of the DK model, one does not, in principle, need a particular ordering relation between $E$ and $B$. In fact, for constant and uniform $\mathbf{E}$ and $\mathbf{B}$, the motion of an electron with zero initial energy can be exactly decomposed into a drift and circular motions, the trajectory being a cycloid curve [32]. In this case, the linear (drift) and the circular (referred to as oscillatory below) *speeds* are exactly equal to one another, and equal to $E/B$. Because of that, the drift and the averaged over a time period oscillatory kinetic energy of such an electron are exactly equal as well:

$$W_{\mathrm{osc}} = \frac{m v_{\mathrm{osc}}^2}{2} = \mu B = \frac{m E^2}{2B^2} = \frac{m v_{\mathrm{d}}^2}{2} = W_{\mathrm{d}}, \quad (22)$$

$$\langle W_{\mathrm{tot}} \rangle = \frac{m \langle (\mathbf{v}_{\mathrm{osc}} + \mathbf{v}_{\mathrm{d}})^2 \rangle}{2} = W_{\mathrm{osc}} + W_{\mathrm{d}} = \frac{m E^2}{B^2}. \quad (23)$$

Although in our situation the fields are not constant and uniform, they are very nearly such because of (i) the long timescale of the current pulse; (ii) the small curvature of the cathode surface (in our case, the surface is flat); and (iii) the slow spatial (logarithmic radial) dependence of the electric field. We conclude that we are not justified in neglecting the drift motion kinetic energy of an electron at and around the time of emission. As time goes on, however, an electron drifts toward the load where $E$ is diminishingly small (remembering the load is a conducting short); then it is the other drift that becomes dominant. Correspondingly, we expect that near the load the DK model (and ordering) becomes a better approximation.

The single particle trajectory shown in Fig. 8 demonstrates this point. Initially, the drift motion and oscillatory kinetic energies are about equal, as predicted by Eqs. (22) and (23). Indeed, we observe that the oscillatory kinetic energy, which does not include the drift motion (magenta curve), is about half of the average of the full kinetic energy (blue curve), and after adding the drift motion kinetic energy, the average of the full kinetic energy is reached (green dashed curve). We also see that later in time, the drift motion kinetic energy becomes negligibly small, conforming to the DK ordering. Figure 8 shows that regardless of when a particle is initialized, at the three times 7.5, 10, and 15 ns, the energy balance discussed above holds. In conclusion, although the drift motion kinetic energy is not in the formal drift kinetic model, to properly account for the energy balance and comparison between drift and full kinetic models, it must be added to the total kinetic energy of the drift kinetic electrons. A consequence of this is discussed below.

Returning now to Fig. 6, we observe that the drift kinetic simulation shows initially faster rise of the total kinetic energy than the full kinetic one. We already mentioned that the SCL emission near $r = 5$ cm is not completely realistic due to the sharp emitting boundary, causing emission of particles with large energies. These high energy particles propagate quickly radially inward (due to the large initial $\mathbf{E} \times \mathbf{B}$ drift) and create a high energy population of electrons, distributed throughout the whole SCL layer, including at small radii where SCL emission does not occur. In principle, the same should be true for both the drift kinetic and full kinetic particles. However, full kinetic particles with high energy (momentum) have a large Larmor radius, whereas drift kinetic particles are always assumed to have zero Larmor radius. As a result, full kinetic particles with large Larmor radii get intercepted by either the absorber or the cathode surface, whereas drift kinetic particles of similar energy remain in the system, radially propagating inward. In other words, the observed discrepancies in the total charge and kinetic energies are due to the finite Larmor radius effect of *particle-wall interactions*. Another indication that the higher total kinetic energy in the DK simulation comes from this set of particles is that the rise happens quickly after the threshold field is exceeded ($t \gtrsim 7.5$ ns); however, only particles near ($r \simeq 5$ cm) are emitted at these early times since at smaller radii $E_{\mathrm{th}}$ has not yet been exceeded. We have made an attempt to mitigate this problem by selecting a subrange or $r$ values for our analyses, however, there is no way (within our test PIC codes) to downselect these high energy particles within the range of consideration ($3.1 \leq r \leq 4.5$). In fact, looking at the total charge and kinetic energy of particles in the system, shown in Fig. 7, we see that when including the full $r$ range, the particle populations have an even more pronounced differences in the total charge and kinetic energy. It is worth noting that once an electron layer

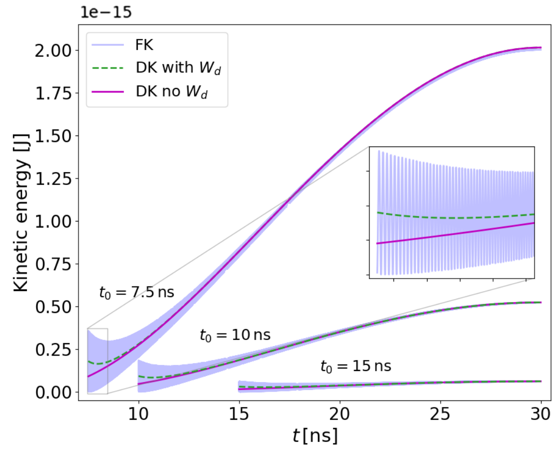


FIG. 8. Comparison between the kinetic energy of a single particle initialized with zero velocity in the full kinetic and drift kinetic models, with and without accounting for the drift motion kinetic energy, $W_d$, for a sine squared current pulse with $I_{\mathrm{peak}} = 2$ MA and $\tau_{\mathrm{peak}} = 30$ ns. The particle was initialized from rest near the cathode at $r_0 = 4$ cm and $z_0 = 2$ mm.

has formed, the active emission of electrons largely ceases since the vortical structures contribute large screening electric fields. We revisit the kinetic energy balance in Sec. V in the context of a hybrid full kinetic and drift kinetic PIC model.

Finally, we can draw a conclusion about the lifetime of an electron in the system with SCL emission, that is, the time between when an electron is emitted from and recaptured by the cathode. We see from the single particle energy balance in Fig. 8 that the drift motion energy quickly diminishes and in about 2–3 ns the dominant kinetic energy is the oscillatory, given by $\mu B$. However, looking at Fig. 6 (bottom panel), we see that past about 15 ns the drift motion energy is essential to account for the energy balance for the remainder of the pulse (green thick curve approximates better the full kinetic energy past about 15 ns than the thick magenta curve). Therefore, we may draw the conclusion that the lifetime of an electron must be less than about 2–3 ns since otherwise the drift motion energy of the electrons would not be adding any significant contribution to the total kinetic energy in the DK model.

So far we have mentioned that the formation of vortices is largely independent of the full kinetic particle gyromotion and have given some evidence to support such claim. In the next section, we set up an exemplar problem that provides deeper insight into the validity of our reduced physics assumptions, the nature of vortex formation, as well as properties, such as vortex spatial dimensions.

## IV. AN EXEMPLAR PROBLEM

In this section we aim to study vortex formation and evolution in a more controlled manner. We use an "exemplar problem" of an electron block of charge (a 3D annular disc), which evolves under both external and/or space charge (self-generated) fields. The electron block is initially placed in the middle of the $(r, z)$ domain and we follow its temporal evolution for a time interval, for which no particles are lost to the domain boundaries. In this way we are able to monitor the properties of total charge and energy conservation/balance as well. We study two cases of external fields: (i) a static magnetic field and zero electric field; and (ii) time dependent magnetic and electric fields. In both cases there is contribution of space charge electric fields, unless otherwise noted. The time dependence of the external fields is again given by Eqs. (16) and (17).

The initial placement of the electron block, which will be used throughout this section, is shown in Fig. 9. In the same figure, we show a reference case of negligible space charge electric field, which is accomplished by choosing a negligibly low number density, $n_0 = 1\ \mathrm{m}^{-3}$. This reference case is useful to compare with later simulations, which include space charge fields. In the simulation in Fig. 9 all particles move independently, as "single particles." In order to use the drift kinetic model, the magnetic field needs to be strong enough, e.g., $B \gtrsim 1$ T. This is accomplished by using a sine squared current pulse with $I_{\mathrm{peak}} = 20$ MA and $\tau_{\mathrm{peak}} = 120$ ns, and additionally imposing a threshold value of $E_{\mathrm{th}} = 24$ MV/m. When particles are "released" at this nonzero threshold value of the electric field, the magnetic field has a nonzero (and large enough) value as well, according to (16). The magnetic moment of the electrons in Fig. 9 is initialized by $\mu = m_e E^2/2B^3$, with field values calculated at the time of particle release and at the particle location (thus, at the time of emission $E = E_{\mathrm{th}}$). Notice that at the end of the simulation at 50 ns, particles with the largest weight (yellow color), which start moving farthest from the load, end up closest to the load. This is expected: the threshold value $E_{\mathrm{th}}$ is first exceeded at the largest radial location, which means these particles become "active" first. The effect of the $\nabla B$ drift is seen as well in the slightly curved up particle trajectories, mostly comprised of "yellow" particles in the figure. The relative importance of the two drifts is also seen, with the $\mathbf{E} \times \mathbf{B}$ drift appearing as dominant over the $\nabla B$.

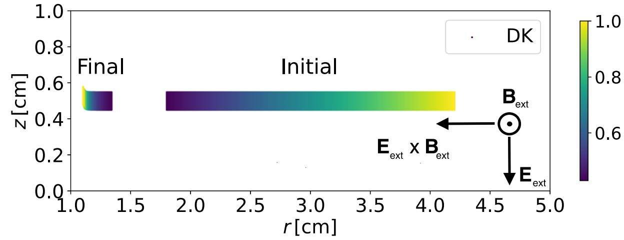


FIG. 9. Drift kinetic propagation of a block of charge without space charge fields in a sine squared current pulse with $I_{\mathrm{peak}} = 20$ MA and $\tau_{\mathrm{peak}} = 120$ ns (particle scatterplot). Particles are released after the electric field exceeds $E_{\mathrm{th}} = 24$ MV/m. The final time of the simulation is 50 ns.

The next simulation in Fig. 10 assumes static magnetic field generated by a constant 150 kA current ($B = 3$ T at $r = 1$ cm) and an initial electron density of $n_0 = 10^{16}\ \mathrm{m}^{-3}$.[3] Particles are initialized with zero energy. In this setup, the electric field is due to the space charge alone, i.e., no external electric field is imposed. The direction of the electric field is toward the block of charge, with opposite directions on opposite sides of the block. The main effect is again due to the $\mathbf{E} \times \mathbf{B}$ drift and manifests in twisting the block ends in opposite directions relative to its middle at 3 cm. What is notable in this simulation is the excellent agreement, particle for particle, between the full kinetic simulation (done with CHICAGO) and the DK-PIC test code (top panel). Similar excellent agreement is observed in the long time evolution in a simulation with a larger number of particles, initialized with random initial positions (bottom panel). However, the most remarkable feature of this (bottom panel) plot is the fact that the initial rectangular electron block can now be seen to have formed a vortex.

[3]The reason for the somewhat low density here is that it avoids certain finite Larmor radius effects, see Fig. 11 below.

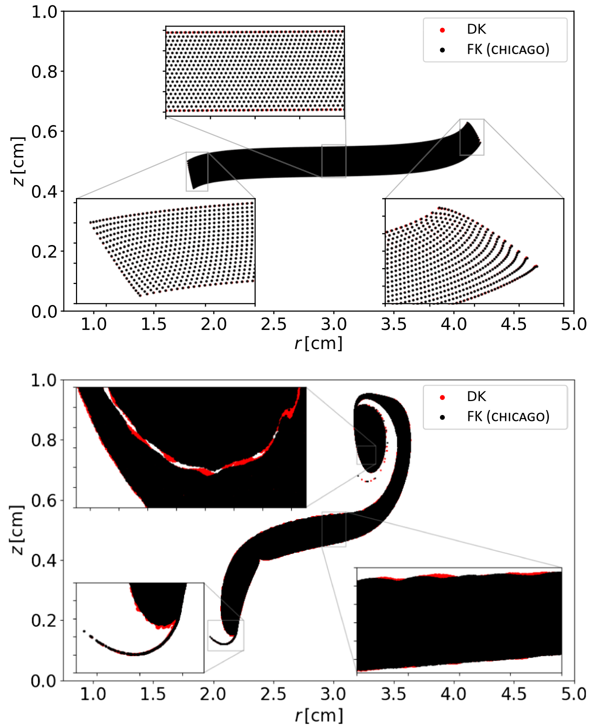


FIG. 10. Comparison of drift kinetic and full kinetic (CHICAGO) time evolution of a block of charge in a static magnetic field. Particle scatterplot at $t = 9$ ns (top panel) with uniform initial particle placement ($N_p = 9600$) and at $t = 100$ ns (bottom panel) with random initial particle placement ($N_p = 1,008,000$). The space charge effect manifests in the S-shape of the electron block of charge due to the combined $\mathbf{E} \times \mathbf{B}$ and $\nabla B$ drifts. At the later time (random initial particle placement, bottom panel), while we still observe excellent agreement between FK and DK models, the main mechanism of vortex formation in SCL emission in both models becomes evident.

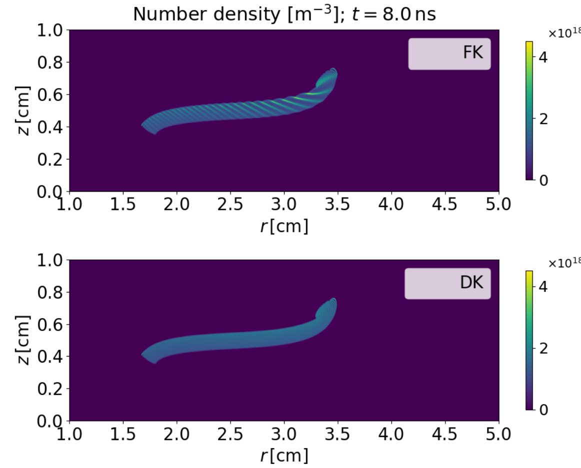


FIG. 11. Manifestation of finite Larmor radius effects in a full kinetic model (top panel), not captured by the drift kinetic model (bottom panel), for a sine squared current pulse simulation with $I_{\text{peak}} = 2$ MA and $t_{\text{peak}} = 30$ ns, initialized at $t_0 = 7.5$ ns.

This illustrates the main mechanism behind vortex formation in the inner MITL: The main contributing factor in this process stems from the $\mathbf{E} \times \mathbf{B}$ drift. In other words, when particles are strongly magnetized, the fully kinetic particle gyromotion is not the determining factor in vortex formation.

Finite Larmor radius (FLR) effects can be present, however, as shown in Fig. 11, where the electron block of initial density $n_0 = 10^{18}\ \text{m}^{-3}$ was evolved in time from $t_0 = 7.5$ ns to $t = 8$ ns in nonzero external fields of a sine squared current pulse with $I = 2$ MA and $\tau_{\text{peak}} = 30$ ns. The top panel shows a full kinetic simulation with clearly visible striations, while the bottom panel shows a drift kinetic simulation lacking such. This FLR effect seems to be related to the spatial variation of the electrons' Larmor radii and cyclotron periods, due to the spatial variation of both the electric and magnetic fields. For example, the space charge electric field vanishes along a horizontal line through the center of the block and quickly rises to its maximum at the horizontal edges; it also has a strong radial variation. The magnetic field has a radial $1/r$ variation. The field variations occur on a much larger spatial scale (millimeters to centimeters) than the typical Larmor radius (tens of microns) and cause particle orbits to interfere and create the observed "beat wave" pattern in the density. However, we emphasize that these striations do not result from an instability and therefore do not grow to large amplitudes in time. In fact, the opposite is true: as time goes on, the interference effect diminishes due to mixing. It seems plausible that this or another FLR effect would be behind the mechanism of vortex formation, however, our simulations do not support such hypothesis.

Next we show that the reduced model of ES-MS fields and neglecting plasma currents are good approximations for typical densities of $10^{18}$–$10^{20}$ m$^{-3}$, i.e., densities for which the space charge electric fields of the electron block are of the same order as the external electric fields.[4] In Fig. 12, we show a three-way comparison of models in time varying external fields corresponding to a sine squared pulse with $I_{\text{peak}} = 2$ MA and $\tau_{\text{peak}} = 30$ ns. The initial electron density was $n_0 = 10^{18}\ \text{m}^{-3}$. The initial time of motion of all electrons was set to $t_0 = 7.5$ ns. For the CHICAGO simulations, the domain was slightly larger in the radial direction, with launch side at 5.2 cm. In the case of the electromagnetic simulation, the data is plotted at 10.28 ns to account for about 0.28 ns transient time, i.e., for the EM wave to travel to the load, reflect, and travel back to the launch side. The important conclusion from this figure is that for SCL relevant densities and electric fields, the plasma (electron) currents, which are included in the

[4]Due to the larger thickness of the initial electron block, the space charge fields could, in fact, be larger than both the typical external fields and those due to the observed SCL electron vortices.

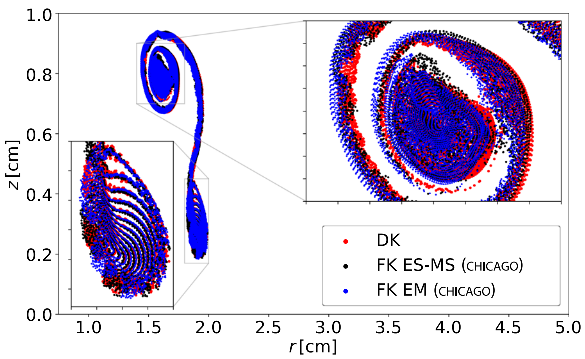


FIG. 12. Three-way model comparison (particle scatterplot): drift kinetic with ES-MS fields (red color), full kinetic with ES-MS fields (black color), and full kinetic with EM fields (blue color) for initial regular particle placement ($N_p = 9600$), with a sine squared current pulse with $I_{\text{peak}} = 2$ MA and $t_{\text{peak}} = 30$ ns, at simulation time $t = 10$ ns.

EM model, do not manifest with any observable effect. Furthermore, effects due to the electromagnetic nature of the fields does not exhibit any observable effects. The last observation is that any finite Larmor radius effects that might be initially present in both ES-MS and EM full kinetic simulations (cf. Fig. 11) diminish quickly in time due to the increasing magnetic field and do not affect the agreement with the drift kinetic model.

We now look at what determines the vortex spatial dimensions. As seen in the previous figures (e.g., Fig. 4), larger vortices form at larger radii and decrease in size at smaller radii, while their average density remains roughly the same. [This appears to be a geometric effect since it is not observed in simulations of SCL emission in a coaxial MITL geometry (not shown).] We posit that the initial thickness, i.e., extent in the $z$-direction, is a determining factor. In Fig. 13 we show density plots of the time evolution of rectangular blocks of charge of varying initial thickness in the range $\Delta z_0 = 100$–$400$ μm in a static magnetic field ($B = 3$ T at $r = 3$ cm). All blocks have the same initial density of $10^{19}\ \mathrm{m}^{-3}$. The left two panels show vortex formation from an initial block 100 μm thick. A full kinetic simulation is shown in the top left panel and a corresponding drift kinetic simulation in the bottom left panel. The right two panels show drift kinetic simulations of blocks of initial thickness 200 μm (top right) and 400 μm (bottom right). Thicker electron blocks have stronger space charge electric fields and break up into vortices sooner. Therefore for clarity, the thinner initial blocks (left two panels) are plotted at final simulation time of 5 ns while the thicker blocks (right two panels) are plotted at 3 ns. From Fig. 13 we observe that the size of vortices is roughly correlated with the initial thickness of the electron block. In the context of SCL emission, we expect to have a larger amount of charge at larger radii since the external electric field increases (logarithmically) with radius [cf. Eq. (17)]. Observing that the average density of vortices does not appear to vary with radius (seen in Fig. 4, for example), a larger amount of charge corresponds to a thicker SCL layer; hence, the observed correlation of vortex sizes with radius.

In closing this section, we give an idea of the energy conserving properties of our FK-PIC and DK-PIC test codes. For representative numbers, we look at the simulations in Fig. 10 (top panel). Since there is no external electric field in this setup, the total (particle kinetic plus field) energy in the system is exactly conserved. At the end of the simulation, at 100 ns, our DK-PIC code had a relative error in the total energy (given by Eq. (12), i.e., *not* including $W_d$) of about $2 \times 10^{-3}\%$; for our FK-PIC code simulation

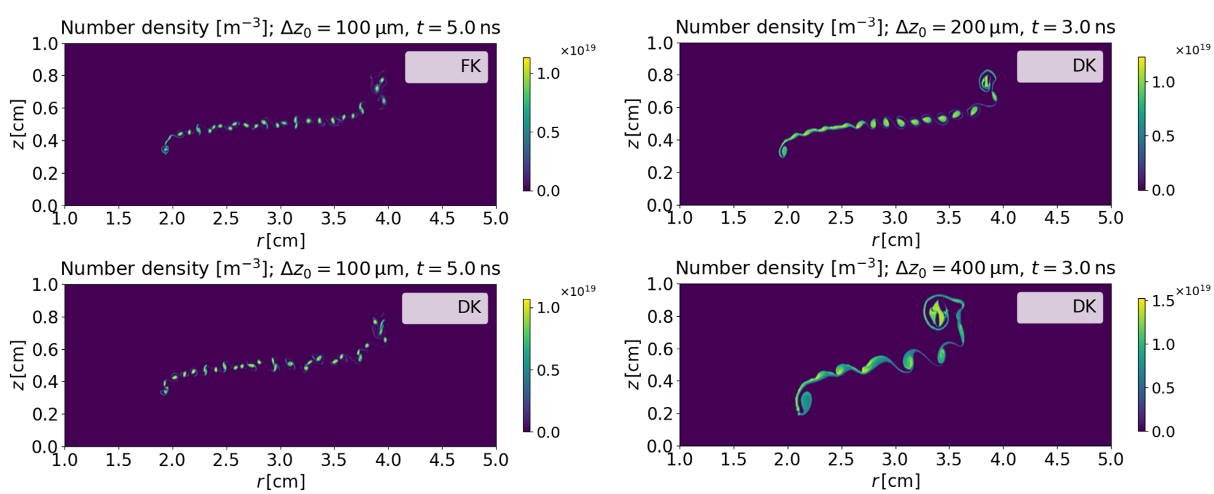


FIG. 13. Time evolution of blocks of charge of varying initial thickness in a static magnetic field. The left two panels compare full kinetic (top) and drift kinetic (bottom) simulations for a 100 μm initial block thickness. The right two panels show drift kinetic density plots for a 200 μm (top) and a 400 μm (bottom) initial block thickness. Correlation between initial thickness and vortex sizes is clearly observed.

(not shown) that number was about $4 \times 10^{-5}\%$. (The expression for the total energy in the full kinetic model is not shown here but can be found in many references, see for example Refs. [19,21,22].)

## V. HYBRID FK/DK PIC MODEL

In Sec. III we noted a discrepancy between the total particle kinetic energy in DK and FK simulations. We now revisit this problem and propose a resolution of the observed disagreement.

The main reason for disagreement between the total kinetic energy of electrons in full kinetic and drift kinetic simulations was identified as the breakdown of the drift kinetic model due to particle-wall interactions. This suggests that a hybrid method, which allows for the simultaneous use of FK and DK particles, may be more appropriate. Here we propose such model, where electrons are initialized as fully kinetic and then converted to drift kinetic according to certain criteria. Possible criteria for conversion include requirements such as cyclotron period being short compared to current pulse length, Larmor radius being small compared to various scale lengths such as system size, gradient scales of electric and magnetic fields, etc. For the present purposes, we use a very simple criterion, by which conversion of a full kinetic particle to a drift kinetic one takes place when the kinetic particle's Larmor radius becomes less than 10 μm. The choice 10 μm is suggested by a few observations. First, typical vortex dimensions are 100–300 μm, much larger than 10 μm. Second, the system size of our radial MITL geometry is a few millimeters (AK gap), also much larger than 10 μm. Other criteria for conversion will be explored in the future, such as comparison of the Larmor radius to gradient scale lengths of electric and magnetic fields, which may become important for nontrivial geometries with sharp corners or edges, etc.

For each particle, once the chosen criterion is satisfied, we use a numerical calculation of the magnetic moment and the drift velocities from a full kinetic electron, which is then converted to a drift kinetic one. The spatial location of the new DK electron is chosen at the position of the full kinetic one. One may propose initializing a drift kinetic electron at the guiding center. However, we have found that suddenly shifting the position of a newly initialized DK particle, compared to its former FK position, creates microscopic charge imbalances, which may lead to certain microscopic instabilities, either physical or numerical. Another aspect of this conversion is that ideally one would implement not only a FK → DK conversion but the opposite one too, i.e., DK → FK. The latter conversion is easy and only relies on a choice of a random direction of the perpendicular to **B** velocity, i.e., a random phase. We have not implemented such reverse transition, leaving this for the future as well.

Simulations with this hybrid method do not noticeably alter the vortex structures, as confirmed by a similar Fourier analysis to that in Sec. III (not shown). However, now comparing the total charge (top panel) and particle kinetic energies (bottom panel) in Fig. 14, we see a very significant improvement in the agreement. We again confirm that including the drift motion kinetic energy, $W_{\rm d}$, is essential.

Finally, regarding the computational efficiency of the hybrid model, in Fig. 15, we plot the fractions of fully kinetic and drift kinetic computational particle counts in time (the average of an ensemble of ten simulations). We see that fully kinetic particles dominate the computation at the very beginning of the current pulse (the simulation starts at $t_0 = 7.5$ ns). However, 2.5 ns later, at 10 ns, their fraction quickly drops to only 7.4% of the total and reaches a (local) maximum of 8.5% at ∼12.7 ns. At about 20 ns their count drops to zero. The drift kinetic particles

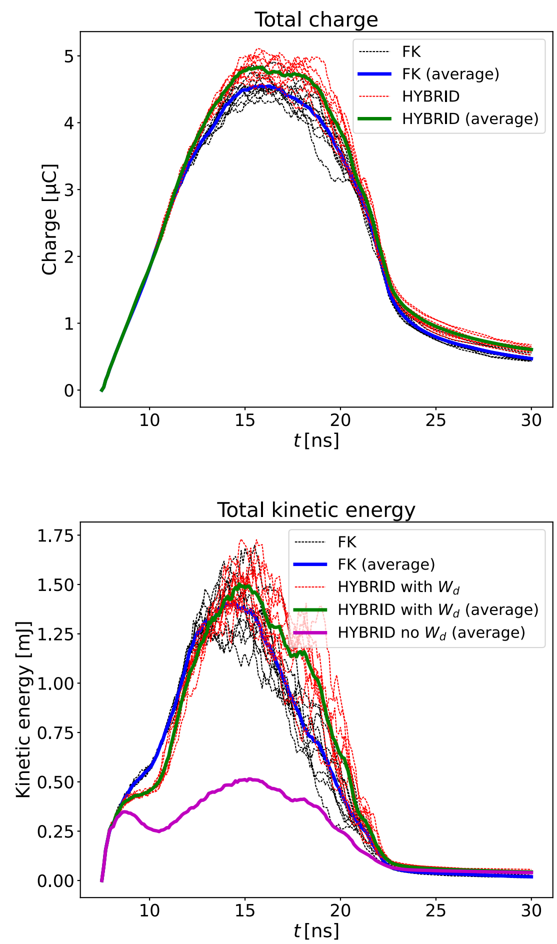


FIG. 14. Comparison of total charge (top panel) and total particle kinetic energy (bottom panel) in full kinetic and hybrid FK/DK simulations with $I_{\rm peak} = 2$ MA and $\tau_{\rm peak} = 30$ ns. The thick lines are the averages of ten simulations with random emission positions.

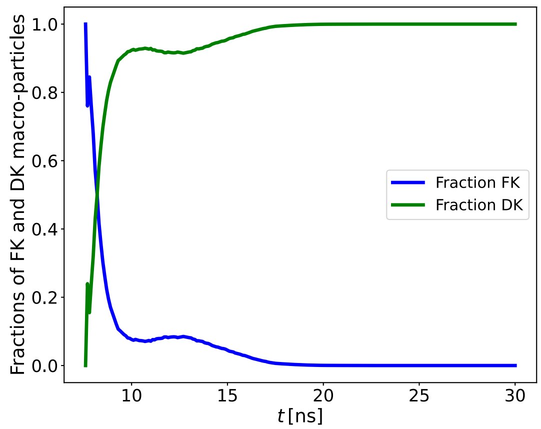


FIG. 15. Computational particle balance in a hybrid simulation with a sine squared current pulse with $I_{\mathrm{peak}} = 2$ MA and $\tau_{\mathrm{peak}} = 30$ ns. The plotted fractions are the averages of ten simulations with random emission positions.

dominate throughout most of the pulse, including around the peak of the current (and the magnetic field), where they provide the biggest computational advantage. Since the limitation on the simulation time step is (primarily) due to fully kinetic electrons, one sees that a large potential for numerical advantage exists in the hybrid method as well.

Realizing this potential has not been exploited in the present work, however, we envision a few directions for future work: (i) using a fixed time step for all particles, such that it resolves fully kinetic particle motion up to the time when their count drops to zero, e.g., 20 ns in our example. One could be more optimistic and force a conversion of all kinetic particles earlier, when their number becomes sufficiently small, say less than 1%–2% of the total number. Once all particles are drift kinetic, the time step could be increased by a large factor for the rest of the simulation (as long as other relevant physics is still adequately resolved). This approach is perhaps the easiest to implement but would not realize the full potential for savings; (ii) subcycling; for example, within one basic drift-kinetic (and field advance) time step, fully kinetic particles taking 20 time steps at fractional $1/20$th of the basic time step. This approach, in our opinion, has the potential to provide larger savings than the previous option, although it may require extra care with respect to the numerical details, such as stability and accuracy. An adaptive time step within either option would provide even further advantage.

The validity of the proposed model should be verified on a case by case basis. Implementing and quantifying the numerical advantages of the hybrid model in different geometries and for more physically realistic current pulses are presently underway within the general code CHICAGO and will be reported in a future publication.

## VI. CONCLUSIONS

In this work we have proposed a method for efficient particle simulations of SCL emission, based on reduced physics models. The applicability of such models must be determined for any one particular device. We have presented numerical evidence, in a simple radial geometry, that Sandia's $Z$ machine is a good candidate for this approach, for typical operational parameters. We have shown that typical observed electron vortices in simulations of SCL emission from the cathode, due to field stress, are reproduced with excellent accuracy in both space and time in a PIC method using the reduced models. The potential for computational cost savings was shown to be significant, of the order of tens to hundreds of times compared to present electromagnetic, fully kinetic PIC simulations.

By studying an exemplar problem of an electron block of charge, we have found that the main mechanism of vortex formation is predominantly due to the space charge (self-generated) electric field and its $\mathbf{E} \times \mathbf{B}$ drift, and that the electron cyclotron motion does not play a significant role in the vortex formation.

The drift kinetic model breaks down in particle-wall interactions, which manifests in a discrepancy between the total kinetic energy of electrons in the FK and DK models. To eliminate this problem, we have proposed a hybrid, fully kinetic and drift kinetic model, where particles are emitted as fully kinetic and converted to drift kinetic according to certain criteria. The kinetic energy discrepancy is thus resolved while the approach still offers a large potential for computational cost savings.

By studying vortex formation in a Cartesian geometry (not presented in this work) we have found that vortex formation in thin strips or layers of charge is independent of the radial geometry convergence effect, or any other external influences. We have tentatively concluded that it is likely related to a velocity shear type instability, similar to the Kelvin-Helmholtz, diocotron, magnetron, etc., instabilities in non-neutral plasma cross-field devices [33–35]. Large vortices formed by these instabilities can establish another possible channel for current loss via conduction currents. The possibility of instability in such flows was also pointed out in Ref. [24]. We are unaware of a stability calculation of radially converging equilibria with zero azimuthal flow and leave detailed investigations for the future.

In light of this, we may conclude that parapotential SCL equilibria [8,9] are unlikely to occur in certain experiments, such as on Sandia's $Z$ machine. At the same time, theories based on parapotential equilibria, such as the flow impedance approach of Ref. [36], have been successful to predict SCL current for a variety operational machine parameters. In order to broaden their scope of applicability, revisions to these theories have been proposed [37]. Based on our SCL vortex formation conclusions, it seems appropriate to seek further refinement of these theories for nonequilibrium SCL layers.

## ACKNOWLEDGMENTS

The authors acknowledge useful feedback and discussions of the manuscript with A. Robinson and S. Slutz from SNL. This work was funded in part by Laboratory Directed Research and Development Grants No. 299292 and No. 226348. Sandia National Laboratories is a multimission laboratory managed and operated by National Technology & Engineering Solutions of Sandia, LLC, a wholly owned subsidiary of Honeywell International Inc., for the U.S. Department of Energy's National Nuclear Security Administration under Contract No. DE-NA0003525. This paper describes objective technical results and analysis. Any subjective views or opinions that might be expressed in the paper do not necessarily represent the views of the U.S. Department of Energy or the U.S. Government.

[1] D. B. Sinars, M. A. Sweeney, C. S. Alexander, D. J. Ampleford, T. Ao, and J. P. Apruzese *et al.*, Review of pulsed power-driven high energy density physics research on Z at Sandia, Phys. Plasmas, **27**, 070501 (2020).

[2] R. D. McBride, W. A. Stygar, M. E. Cuneo, D. B. Sinars, M. G. Mazarakis, and J. J. Leckbee *et al.*, A primer on pulsed power and linear transformer drivers for high energy density physics applications, IEEE Trans. Plasma Sci. **46**, 3928 (2018).

[3] W. A. Stygar, H. C. Ives, D. L. Fehl, M. E. Cuneo, M. G. Mazarakis, and J. E. Bailey *et al.*, X-ray emission from $z$ pinches at $10^7$A: Current scaling, gap closure, and shot-to-shot fluctuations, Phys. Rev. E **69**, 046403 (2004).

[4] M. R. Gomez, R. M. Gilgenbach, M. E. Cuneo, C. A. Jennings, R. D. McBride, E. M. Waisman *et al.*, Experimental study of current loss and plasma formation in the $Z$ machine post-hole convolute, Phys. Rev. Accel. Beams **20**, 010401 (2017).

[5] N. Bennett, D. R. Welch, C. A. Jennings, E. Yu, M. H. Hess, B. T. Hutsel *et al.*, Current transport and loss mechanisms in the Z accelerator, Phys. Rev. Accel. Beams **22**, 120401 (2019).

[6] M. H. Hess and E. G. Evstatiev, Electron dynamics within a MITL containing a load, IEEE Trans. Plasma Sci. **49**, 3398 (2021).

[7] R. V. Lovelace and E. Ott, Theory of magnetic insulation, Phys. Fluids **17**, 1263 (1974).

[8] J. M. Creedon, Relativistic brillouin flow in the high $\nu/\gamma$ diode, J. Appl. Phys. **46**, 2946 (1975).

[9] J. M. Creedon, Magnetic cutoff in high-current diodes, J. Appl. Phys. **48**, 1070 (1977).

[10] C. W. Mendel Jr., Planar one-dimensional magnetically insulated electron flow for arbitrary canonical momentum distribution, J. Appl. Phys. **50**, 3830 (1979).

[11] C. W. Mendel Jr., D. B. Seidl, and S. A. Slutz, A general theory of magnetically insulated electron flow, Phys. Fluids **26**, 3628 (1983).

[12] M. S. Di Capua, Magnetic Insulation, IEEE Trans. Plasma Sci. **11**, 205 (1983).

[13] P. F. Ottinger and J. W. Schumer, Rescaling of equilibrium magnetically insulated flow theory based on results from particle-in-cell simulations, Phys. Plasmas **13**, 063109 (2006).

[14] D. R. Welch, D. V. Rose, R. E. Clark, T. C. Genoni, and T. P. Hughes, Implementation of an non-iterative implicit electromagnetic field solver for dense plasma simulation, Comput. Phys. Commun. **164**, 183 (2004).

[15] D. R. Welch, T. C. Genoni, R. E. Clark, and D. V. Rose, Adaptive particle management in a particle-in-cell code, J. Comput. Phys. **227**, 143 (2007).

[16] T. C. Genoni, R. E. Clark, and D. R. Welch, A fast implicit algorithm for highly magnetized charged particle motion, The Open Plasma Phys. J. **3**, 36 (2010).

[17] D. R. Welch, N. Bennett, T. C. Genoni, D. V. Rose, C. Thoma, C. Miller, and W. A. Stygar, Electrode contaminant plasma effects in $10^7$-A $Z$ pinch accelerators, Phys. Rev. Accel. Beams **22**, 070401 (2019).

[18] D. R. Welch, N. Bennett, T. C. Genoni, C. Thoma, and D. V. Rose, Fast hybrid particle-in-cell technique for pulsed-power accelerators, Phys. Rev. Accel. Beams **23**, 110401 (2020).

[19] E. G. Evstatiev, Application of the phase space action principle to finite-size particle plasma simulations in the drift-kinetic approximation, Comput. Phys. Commun. **185**, 2851 (2014).

[20] M. S. Di Capua and D. G. Pellinen, Propagation of power pulses in magnetically insulated vacuum transmission lines, J. Appl. Phys. **50**, 3713 (1979).

[21] C. K. Birdsall and A. B. Langdon, *Plasma Physics via Computer Simulation*, Series in Plasma Physics (Taylor & Francis, New York, 2005), 1st ed.

[22] R. W. Hockney and J. W. Eastwood, *Computer Simulation Using Particles* (CRC Press, Boca Raton, 2021).

[23] E. G. Evstatiev and B. A. Shadwick, Variational formulation of particle algorithms for kinetic plasma simulations, J. Comput. Phys. **245**, 376 (2013).

[24] Y. Y. Lau, D. A. Packard, C. J. Swenson, J. W. Luginsland, D. Li, A. Jassem, N. M. Jordan, R. D. McBride, and R. M. Gilgenbach, Explicit Brillouin flow solutions in magnetrons, magnetically insulated line oscillators, and radial magnetically insulated transmission lines, IEEE Trans. Plasma Sci. **49**, 3418 (2021).

[25] A. M. Darr and K. L. Cartwright, Mutually magnetically insulated two-species Brillouin flow, Phys. Plasmas **30**, 053105 (2023).

[26] R. G. Littlejohn, Variational principles of guiding centre motion, J. Plasma Phys. **29**, 111 (1983).

[27] J. J. Watrous, J. W. Luginsland, and G. E. Sasser, An improved space-charge-limited emission algorithm for use in particle-in-cell codes, Phys. Plasmas **8**, 289 (2001).

[28] J. W. Luginsland, Y. Y. Lau, R. J. Umstattd, and J. J. Watrous, Beyond the Child–Langmuir law: A review of recent results on multidimensional space-charge-limited flow, Phys. Plasmas **9**, 2371 (2002).

[29] J. P. Boris, Relativistic plasma simulation–optimization of a hybrid code, in *Fourth Conference on Numerical Simulation of Plasmas* (Naval Research Laboratory, Washington, DC, 1970), pp. 3–67.
[30] E. Hairer, G. Wanner, and C. Lubich, *Geometric Numerical Integration*, Springer Series in Computational Mathematics Vol. 31 (Springer, Berlin, Heidelberg, 2002).
[31] N. A. Roberds, K. L. Cartwright, A. J. Sandoval, K. R. C. Beckwith, E. Cyr, and F. W. Glines, Numerical simulation of a relativistic magnetron using a fluid electron model, Phys. Plasmas **29**, 083104 (2022).
[32] J. C. Slater, Microwave electronics, Rev. Mod. Phys. **18**, 441 (1946).
[33] O. Buneman, R. H. Levy, and L. M. Linson, Stability of crossed field electron beams, J. Appl. Phys. **37**, 3203 (1966).
[34] R. C. Davidson, H.-W. Chan, C. Chen, and S. Lund, Equilibrium and stability properties of intense non-neutral electron flow, Rev. Mod. Phys. **63**, 341 (1991).
[35] R. C. Davidson, *Physics of Nonneutral Plasmas* (World Scientific Publishing Company, Singapore, 2001).
[36] C. W. Mendel, Jr. and S. E. Rosenthal, Modeling magnetically insulated devices using flow impedance, Phys. Plasmas **2**, 1332 (1995).
[37] P. F. Ottinger and J. W. Schumer, Magnetically insulated ion flow theory, Phys. Plasmas **13**, 063101 (2006).